JOURNAL OF SOLID STATE CHEMISTRY 7, 428–447 (1973)

Interpretation of Structure and Magnetism in Transition-Metal Pnictides M_2X and $(M_{1-x}M'_x)_2X$*

J. B. GOODENOUGH

Lincoln Laboratory, Massachusetts Institute of Technology, Lexington, Massachusetts 02173

Received October 27, 1972

The transition-metal pnictides M_2X and $(M_{1-x}M'_x)_2X$ containing first-row transition elements and X = P, As or Sb tend to crystallize in three related structures that permit metal-metal bonding via partially filled 3*d*-shell cores. It is argued that in the phosphides, and probably in most arsenides and antimonides, of the first-row transition elements, the X-atom *p* bands are filled and the cation 4*s* bands are empty, so that the number of 3*d* electrons per metal atom are known unambiguously. Furthermore, some of the phosphides are magnetic and some are not, so that the width of the 3*d*-electron bands can be varied by As substitution or by hydrostatic pressure to provide critical information about changes in magnetic order, magnetic-ordering temperatures, and the magnitudes of the atomic moments as a function of bandwidth and band occupation in the critical region where the transition from spontaneous magnetism to Pauli paramagnetism occurs. General conceptual phase diagrams are developed from physical arguments about the influence of electron–electron correlations on quasidegenerate, narrow *d* bands. This discussion, which leads to an explanation of the Slater–Pauling curve of magnetization vs electron/atom ratio in the transition metals, is then applied to an interpretation of available magnetic data for the transition-metal pnictides M_2X and $(M_{1-x}M'_x)_2X$. Prediction of individual atomic moments requires that allowance be made for distinguishable cation sites and for the transfer of 3*d*-electron charge from lighter to heavier elements, but the crystal-field effects appear to be manifest only in the signs of the interatomic exchange interactions. Significantly, in alloys an equal and integral number of majority-spin electrons tend to be stabilized at each atomic constituent that is magnetic.

I. Introduction

In order to study experimentally the changes with bandwidth and band occupation of itinerant-electron magnetism, it is first essential to identify suitable materials. The first-row transition metals, although chemically simple, are complicated by an overlapping of partially filled 3*d* and 4*s* bands that renders ambiguous the occupation of the 3*d* bands as well as those physical properties that are imparted solely by the 3*d* electrons. This ambiguity is heightened by the structural changes that accompany variations in the electron-atom ratio, and the problem becomes acute in alloy systems, where the 3*d* bands of solvent and solute arrays are at different energies. Finally, the ability to change the bandwidth without strongly perturbing the system is essentially limited to the influence of hydrostatic pressure. This paper argues that the transition-metal systems $(M_{1-x}M'_x)_2X$, where X = P, As or Sb and M, M′ are first-row transition elements, have magnetic and structural properties determined by the 3*d* electrons and allow a less ambiguous assignment of the total number of 3*d* electrons per molecule. Furthermore, they permit variations of the widths and occupancies of the 3*d*-electron bands via X-atom substitutions as well as hydrostatic pressure. However, they are chemically and structurally somewhat more complicated.

Although holes may be introduced into the outer *p* bands of pnictides or chalcogenides of the first-row transition elements, especially for heavier metal atoms, such holes generally become trapped in antibonding orbitals of an X–X homopolar bond within an X_2 diatomic anion or metalloid atom. The pyrite, marcasite and arsenopyrite MX_2 structures illustrate this

* This work was sponsored by the Department of the Air Force.

Copyright © 1973 by Academic Press, Inc.
All rights of reproduction in any form reserved.
Printed in Great Britain

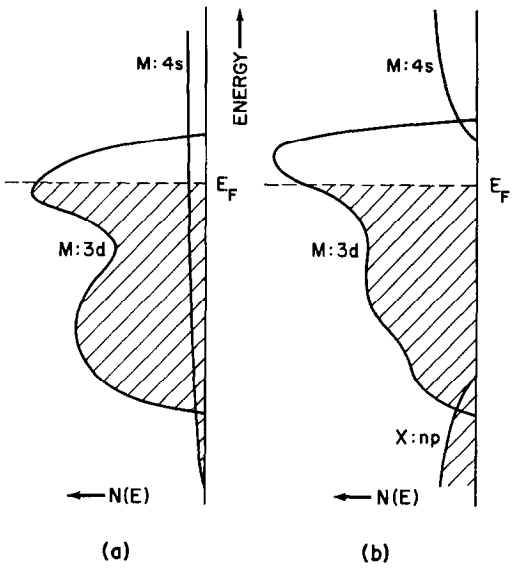

FIG. 1. Overlap of broad-band and narrow-3*d*-band energies for (a) transition metals and (b) transition–metal pnictides M_2X, where N(E) is the density of one-electron states. Also cf. Fig. 7.

principle. More strikingly, the complex covelline structure of CuS represents the formation of $Cu^{2+}S^{2-}\cdot Cu_2^{+}(S_2)^{2-}$, where the valences are formal. In this compound, only two-thirds of the sulfur atoms form diatomic S_2^{2-} anions, which signals the existence of only two-thirds holes per sulfur atom in the sulfur 3*p* bands. The absence of diatomic X_2 clusters in the $(M_{1-x}M'_x)_2X$ structures to be discussed as well as the existence of X–X separations consistent with X^{3-} ions argues against any significant overlap of the X-atom outer *p* bands and the Fermi energy. This conclusion is also consistent with the small formal valences at the metal atoms: $M^{+}M^{2+}X^{3-}$. In this paper we shall assume that introduction of X atoms into a transition-metal array alters the band structure as shown schematically in Fig. 1. The significant feature is a splitting of the non *d*-like electrons about the Fermi energy E_F. The bottom of the empty band is largely transition-metal 4*s*, and the top of the filled bands is largely X-atom outer *p*.

In Section II, three related structures are described, and their relative stabilities are argued in terms of the strength of the metal–metal bonding and anisotropic elastic forces introduced by M-atom ordering and/or crystal-field splittings. The variation of effective M-atom size with atomic number is interpreted on the basis of Fig. 1 and crystal-field effects. Section III develops conceptual phase diagrams from general physical arguments that allow quantitative predictions of spontaneous atomic moments and of the type of magnetic order for different 3*d*-electron/atom ratios. These are used in Section IV to interpret the magnetic properties of several orthorhombic and hexagonal systems $(M_{1-x}M'_x)_2P$, $M_2P_{1-x}As_x$, and $MM'P_{1-x}As_x$. Quantitative deductions about the magnitudes of the atomic moments to be found at different crystallographic sites are summarized in Table II. These can be checked by neutron diffraction.

II. Structural Considerations

Systematic studies of the structures of the transition–metal compounds M_2X and systems $(M_{1-x}M'_x)_2X$ have been reviewed in the literature [*1–4*]. The essential features are summarized here.

Three closely related structures are generally encountered if X = P, As or Sb: the orthorhombic CoP_2 structure [*5*], which represents a distorted form of the filled NiAs structure of Ni_2In [*6*], the hexagonal Fe_2P structure [*7*], and the tetragonal structure of Fe_2As or Cu_2Sb [*8*]. As emphasized by Fruchart *et al.* [*3*], the fundamental building block common to these three

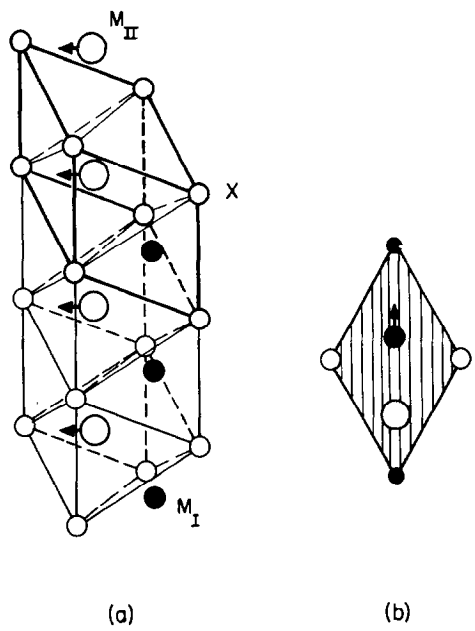

FIG. 2. (a) Edge-shared octahedral sites sharing faces with tetrahedral sites. (b) Elementary $M_IM_{II}X$ rhombus projected onto a basal plane of column. Black and white circles of projection are on alternate basal planes.

TABLE I

STRUCTURAL DATA FOR Co_2P, Fe_2P, Fe_2As AND Cu_2Sb. FROM S. RUNDQVIST, *Acta Chem. Scand.* **14**, 1961 (1960); S. RUNDQVIST AND F. JELLINEK, *Acta Chem. Scand.* **13**, 425 (1959), and M. ELANDER, G. HÄGG AND A. WESTGREN, *Archiv. Kemi. Min. Geol.* **12B**, 1 (1936).

Co_2P: C23 structure. Space Group *Pnma*, four formula units per unit cell, all atoms in positions 4(c).

$a_0 = 5.646$, $b_0 = 3.513$, $c_0 = 6.608$ Å
Molecular volume = 32.8 Å^3

Interatomic distances [Å]: Numbers in parentheses give numbers of atoms.

	Co_I	Co_{II}	P
Co_I:	$2.54_2(2)$	$2.62_4(2)$, $2.66_5(1)$ $2.69_1(2)$, $2.71_2(1)$	2.14(1), 2.23(2) 2.24(1)
Co_{II}:	$2.62_4(2)$, $2.66_5(1)$ $2.69_1(2)$, $2.71_2(1)$	$2.83_6(2)$, 3.035(2)	2.29(1), 2.40(2) 2.54(2)
P:	2.14(1), 2.23(2) 2.24(1)	2.29(1), 2.40(2) 2.54(2)	

2. Fe_2P: C22 structure. Space Group $P\bar{6}2m$, three formula units per unit cell, M_I atoms in (3f), M_{II} in (3g), P_I in (2c), and P_{II} in (1b).

$a_h = 5.865$, $c_h = 3.456$ Å, $c_h/a_h = 0.5893$
Molecular volume = 34.3 Å^3

Interatomic distances [Å]: Numbers in parentheses give numbers of atoms.

	Fe_I	Fe_{II}	P
Fe_I:	2.60(2)	2.63(2), 2.71(4)	2.22(2), 2.29(2)
Fe_{II}:	2.63(2), 2.71(4)	3.08(4)	2.38(1), 2.48(4)
P_I:	2.22(3)	2.48(6)	
P_{II}:	2.29(6)	2.38(3)	

3. Fe_2As and Cu_2Sb: C38 structure. Space Group *P4/nmm*, two formula units per unit cell, M_I atoms in 2(a), M_{II} and X atoms in 2(c).

Fe_2As: $a_t = 3.627$, $c_t = 5.973$ Å, $c_t/a_t = 1.65$. Molecular volume = 39.3 Å^3
Cu_2Sb: $a_t = 3.992$, $c_t = 6.091$ Å, $c_t/a_t = 1.53$. Molecular volume = 48.53 Å^3

Interatomic distances [Å]: Numbers in parentheses give numbers of atoms.

	Fe_I	Fe_{II}	As		Cu_I	Cu_{II}	Sb
Fe_I:	2.57(4)	2.69(4)	2.40(4)	Cu_I:	2.82(4)	2.59(4)	2.70(4)
Fe_{II}:	2.69(4)		2.41(1) 2.60(4)	Cu_{II}:	2.59(4)		2.62(1) 2.83(4)
As:	2.40(4)	2.41(1) 2.60(4)		Sb:	2.70(4)	2.62(1) 2.83(4)	

structures is the rhombohedral $M_IM_{II}X$ subcell of Fig. 2. These subcells are stacked on top of one another to form columns running parallel to the short axis—unit length shown in Fig. 2—of the crystallographic cell. The three related crystallographic structures are built up from three different packings of these columns, as is illustrated in Figs. 3–5. The columns run parallel

TABLE II

POSSIBLE STABLE ITINERANT-ELECTRON ATOMIC MOMENTS, IN BOHR MAGNETONS, PREDICTED FOR FERROMAGNETIC TRANSITION-METAL PNICTIDES $(M_{1-x}M'_x)_2X_{1-y}X'_y$. MOMENTS INFERRED FROM MAGNETIZATION DATA FOR DIFFERENT SYSTEMS ARE ITALIC.

	M_I	M_{II}
Cr:	$0, (0.5-\delta)$	$0, (0.5+\delta)^a$
Mn:	$0, (0.5-\delta)$	$0, (0.5+\delta), (2.5+\delta)^b$
Fe:	$0, (1.5-\delta)^c$	$0, (1.5+\delta)$
Co:	$0, (0.5-\delta), (2.5-\delta)$	$0, (0.5+\delta), (2.5+\delta)$
Ni:	0	0

In phosphides, $\delta \approx 0.17 \pm 0.3$ for like-atom M_I–M_{II} pairs, $\delta = \delta' \approx 0.25 \pm 0.3$ for atomic numbers $(Z_I - Z_{II}) = 1$, and $\delta = \delta^* \approx 0.58 \pm 0.03$ for atomic numbers $(Z_I - Z_{II}) = 2$. In arsenides, the values of δ are larger (by about 0.1).

[a] Also observe $0 < \mu_{II}^{Cr} < (0.5+\delta)$.

[b] Predicted only for alloys in which four majority-spin electrons per atom matches configuration at atoms of the other constituent.

[c] Also observe $0 \leq \mu_I^{Fe} \leq (1.5-\delta)$.

to the orthorhombic b_o axis, the hexagonal c_h axis, or the two tetragonal a_t axes.

Each column consists of edge-shared X-atom octahedra and, on either side, of the tetrahedra formed by the two ends of the common edge and the two apices of two neighboring octahedra. The tetrahedral-sites on one side only are occupied, by M_I atoms. The M_{II} atoms are displaced from the center of the octahedral sites toward the apex most removed from the M_I atoms. This displacement elongates the octahedral site and gives the M_{II} atoms a square-pyramid X-atom coordination. Nevertheless, the M_I–M_{II} distance is short enough (~ 2.63 Å in Co_2P and Fe_2P, see Table I) for the formation of itinerant 3*d*-electron orbitals in the zig-zag M_I–M_{II} chains within a column.

The orthorhombic structure of Fig. 3(a) may be compared with the Ni_2In structure of Fig. 3(b). Orthorhombic packing of the columns of Fig. 2 gives common "octahedral-site" faces along a_o, common edges along c_o. Displacement of the M_{II} atoms from the centers of the octahedra produces one set of zig-zag M_{II} chains running parallel to a_o in the c_o–a_o plane, and another set running parallel to b_o via edge-shared square pyramids. (In the Ni_2In structure, the octahedra are not distorted, and the M_{II} ions of face-shared octahedra form linear chains.) Ortho-

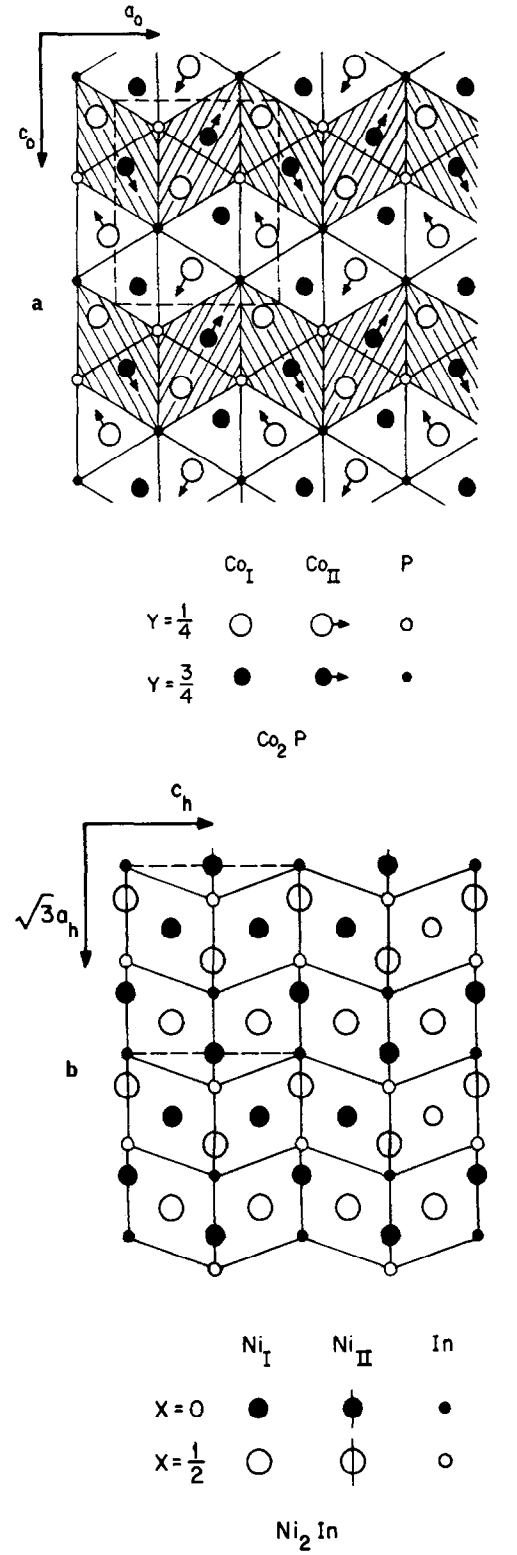

FIG. 3. (a) Orthorhombic Co_2P structure projected onto a_o-c_o plane. (b) Hexagonal Ni_2In structure projected onto (100) plane.

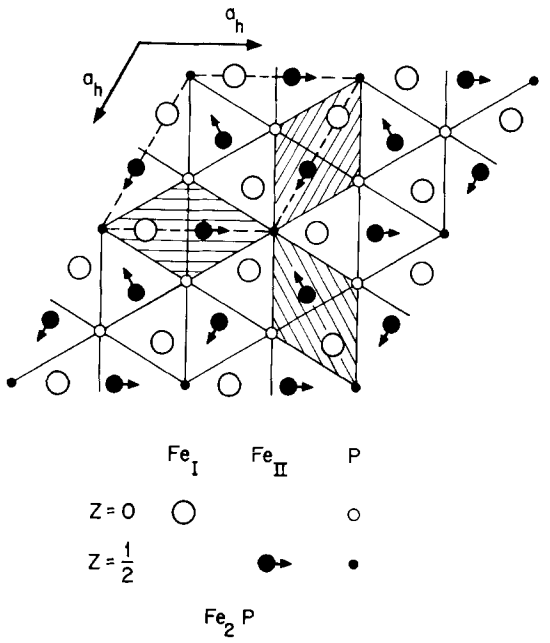

FIG. 4. Hexagonal Fe_2P structure projected onto basal plane.

rhombic packing also produces shared tetrahedral-site faces, and in the Co_2P structure an M_I atom occupies one of these paired sites. (In the Ni_2In structure, the M_I atom occupies the shared face—and hence a trigonal-bipyramid site). In Co_2P, the M_I atoms form zig-zag chains parallel to b_o via edge-shared tetrahedra, and the M_I–M_I separations (2.54 Å) within these chains are even shorter than the M_I–M_{II} separations within a column. In the a_o–c_o plane, M_I–M_{II} pairs are formed via a common polyhedral face, and this M_I–M_{II} separation (2.66_5 Å) is only slightly larger than the similar M_I–M_{II} distance of the zig-zag chains parallel to b_o within the columns. Zig-zag M_I–M_{II} chains parallel to b_o are also formed via a common pyramidal and tetrahedral edge. In these chains the M_I–M_{II} separation is 2.69_1 Å. The remaining short M_I–M_{II} separation (2.71_2 Å) is between a tetrahedral and a pyramidal site sharing a common edge in the c_o–a_o plane.

Hexagonal packing of the columns of Fig. 2 creates triangular M_I clusters in the basal planes about a common edge parallel to c_h. The M_I–M_I separations within these clusters is comparable to the short M_I–M_I distances of Co_2P. Parallel to b_o, M_I–M_{II} bonds are formed via shared tetrahedral and pyramidal edges, and the bond lengths are comparable to the similar bonds in Fe_2P. The principal difference between the M_I–M_{II} bonding in the hexagonal and orthorhombic structures is two vs three shared polyhedral faces and four vs three shared polyhedral edges per molecule. Although hexagonal packing produces four—as against two—shared octahedral-site faces per molecule, the M_{II} displacements do not create shared pyramidal faces, and the corresponding M_{II}–M_{II} separations are relatively large (3.08 Å in Fe_2P and 3.03_5 in Co_2P). The M_{II}–M_{II} bond length (2.83 Å) via a shared pyramidal-site edge, which occurs in zig-zag chains parallel to b_o in Co_2P, allows stronger M_{II}–M_{II} bonding in the orthorhombic phase. As emphasized by Rundqvist [*1*], the X-atom polyhedra are similar in both structures. Therefore, it would appear that the relative energies of the two depend upon the ratio of the energy gained by enhanced metal–metal bonding vs the elastic energy lost by lowering the symmetry from hexagonal to orthorhombic.

The structures and molecular volumes of the

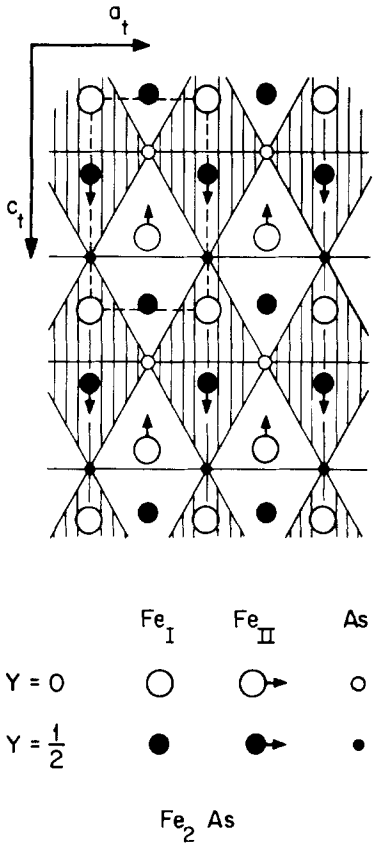

FIG. 5. Tetragonal Fe_2As or Cu_2Sb structure projected on c_t-a_t plane.

phosphides and arsenides, as given by Roy-Montreuil *et al.* [4], are presented in Fig. 6. With the sole exception of Co_2P itself, the orthorhombic phase is not found in M_2X compounds. This observation indicates that unless there is some mechanism present to introduce anisotropic elastic forces, the hexagonal phase is the more stable. Evidence for anisotropic forces associated with the Co atoms comes from Co_2As, which has a deformed-hexagonal structure. However, if this inference is correct, then MM'X compounds that order the M and M' atoms in the two types of sites could have the anisotropic elastic forces required for stabilization of the orthorhombic phase. Significantly, ordering of M and M' ions has been shown to be virtually complete in MnFeP, CrFeP and MnCoP; to be pronounced in FeCoP; and to be weaker in the compounds containing nickel: MnNiP, FeNiP, and CoNiP [3]. It would be useful to know whether there is a difference in the atomic ordering of the hexagonal and orthorhombic phases of MnNiP and MnNiAs.

The hypothesis advanced by Roy-Montreuil *et al.* [4], that the orthorhombic phase is associated with enhanced metal–metal bonding, appears to be essentially correct, as is well substantiated by their elegant experiments. It is also consistent with the structural observation of shorter M–M separations in the orthorhombic phase. The 3*d*-electron binding energy to be gained is more likely to exceed the elastic energy lost not only where the elastic energy is reduced by atomic ordering, but also where the overall 3*d*-electron binding energy is high. Therefore, it is quite consistent to find fewer orthorhombic structures among the arsenides, where the M–M separations are larger. What does not necessarily follow is their conclusion [4], which failed to take account of the elastic forces, that the strength of the metal–metal bonding decreases in the order.

$$\text{MnCo} > \text{MnNi} > \text{CrCo or FeCo} > \text{MnFe} > \text{FeFe or MnMn}$$

Strong metal–metal bonding gives a bandwidth that is too large to support spontaneous magnetism. Nevertheless, hexagonal Mn_2P appears to be nonmagnetic (or to have a low ($T_N < 77$ K) Néel temperature) whereas orthorhombic MnCoP is ferromagnetic ($T_c = 583$ K) with essentially all of the magnetization at the Mn atoms. It therefore would appear that in MnCoP it is not an enhanced metal–metal bonding relative to Mn_2P that stabilizes the orthorhombic vs the hexagonal structure, but a change in the elastic energy associated with atomic order.

Variations with x of the lattice parameters of ordered, orthorhombic $(Co_{1-x}Mn_x)_2P$, $0 \leqslant x \leqslant 0.8$, [3] provide evidence that metal–metal bonding between like atoms is strong. For $x \leqslant 0.5$, the structural formula is $Co_I(Co_{1-2x}Mn_{2x})_{II}P$, and b_o remains nearly constant while a_o and c_o increase rapidly with x. The bonds with the smallest component in the a_o-c_o plane are the M_I–M_I bonds, which remain all Co_I–Co_I bonds. For $x > 0.5$, on the other hand, the structural formula is $(Co_{2-2x}Mn_{2x-1})_I Mn_{II}P$, and a_o remains nearly constant while b_o and c_o increase rapidly with x. The bonds with the largest component along a_o are the M_{II}–M_{II} bonds, which remain all Mn_{II}–M_{II} bonds. Thus the bonds between like atoms retain a characteristic length while the lattice adjusts to the introduction of atoms of considerably larger size. This type of accommodation is not possible in the hexagonal phase, which illustrates why the orthorhombic phase is stabilized in ordered systems containing strong metal–metal bonding.

Tetragonal packing of the columns of Fig. 2 creates edge-shared pyramidal and tetrahedral sites in the basal planes, see Fig. 5. In this arrangement, each M_I atom shares tetrahedral-site edges with four M_I near neighbors and polygonal faces with four M_{II} atoms. Thus the number of short M_I–M_I and M_I–M_{II} bonds is increased at the expense of the longer M_{II}–M_{II} bonds. Clearly, the tetragonal phase allows optimization of the metal–metal bonding where the X-atom is too large to permit competitive stabilization of "close" M–M separations in three dimensions. A "close" approach may be defined as one stabilizing band rather than localized (or strongly correlated) 3*d* electrons. Furthermore, the relative stabilities of M_I–M_I vs M_I–M_{II} bonding may be adjusted via the axial ratio c_t/a_t, a fact that may have important ramifications for the properties of magnetic compounds with the tetragonal structure [9].

A plot of effective atomic radius vs atomic number of the M atoms exhibits, according to Fig. 6, minima at Co and perhaps V, with an intermediate maximum at Mn. This behavior reflects 3*d*-electron bonding and antibonding superposed on the normal contraction—given the same number of broad-band electrons—of the 3*d* shell with increasing atomic number. Two types of 3*d* orbitals must be distinguished: those that participate in M–X σ bonding and those that

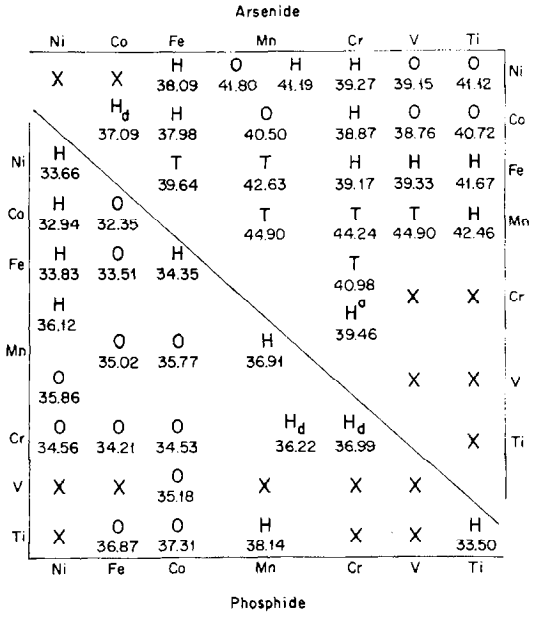

FIG. 6. Structures and molecular volumes for several transition-metal phosphides and arsenides M_2X and MM'X. O = orthorhombic, H = hexagonal, T = tetragonal, and X = not reported.

do not. Let the former be designated d_σ, the latter d_m. The respective bandwidths are w_σ and w_m. With the energy diagram of Fig. 1, the M-atom 3*d* orbitals are antibonding with respect to the M–X bonds, and covalent mixing with the X-atom orbitals destabilizes the 3*d* bands. The d_σ orbitals are destabilized more than the d_m orbitals, and the center of energy of w_σ is higher than that of w_m by the crystal-field splitting Δ. The relative magnitudes of w_σ and w_m depend upon the relative magnitudes of the M–X–M and the M–M interactions. Electrons in the bottom half of the d_m band are in M–M bonding states and reduce the M–M separation. However, those in the bottom half of the d_σ band are in M–X antibonding states and therefore increase the *M–X* bond length—even though the M–X–M interactions are bonding. The initial 3*d* electrons occupy predominantly d_m bonding states, and their M–M binding energy plus the contraction of the 3*d* shell with increasing atomic number insures a decrease in the effective M-atom radius with increasing atomic number. However, at some critical 3*d*-electron concentration, determined by $[\Delta + \frac{1}{2}(w_m - w_\sigma)]/w_m$ and the density of states within the d_m band, the Fermi energy begins to enter an energy domain populated primarily by d_σ states. This is illustrated in Fig. 7, where each band is assumed to have a bimodal density-of-states distribution. Such a distribution is anticipated for orbitals of any zig-zag string, a dominant feature of the M–M interactions. Where the Fermi energy enters the energy domain rich in d_σ states, additional electrons are predominantly (M–X)-antibonding electrons that increase the M–X bond length. This increase may be large enough to offset the 3*d* shell contraction, giving a net increase in effective radius with increasing atomic number. As the Fermi energy enters the upper half of the 3*d* bands, the d_m states are again predominant. Although these are (M–M)-antibonding electrons, the increase in M–M bond length is not significant because the bond length is primarily determined by the M–X distances. Therefore, the 3*d*-shell contraction with increasing atomic number dominates the change in effective M-atom radius.

It is possible to identify three 3*d* orbitals per atom that are active in M–M bonding. This result is independent of whether the structure is orthorhombic, hexagonal or tetragonal. Therefore,

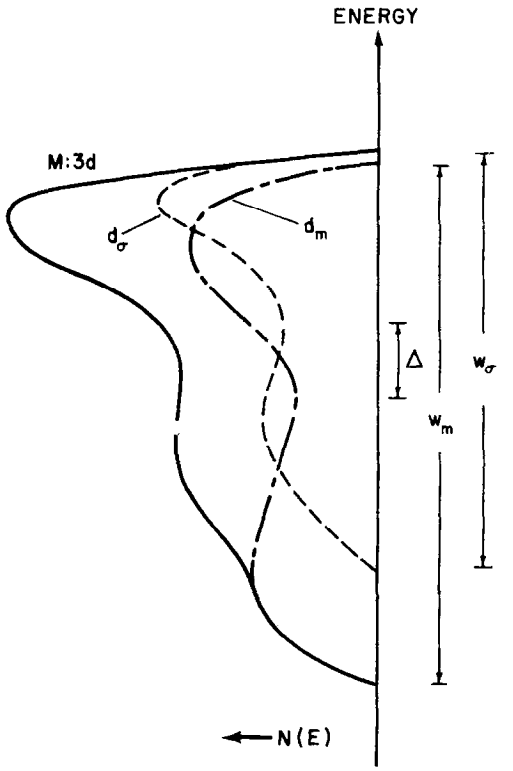

FIG. 7. Schematic density-of-states N(E) vs energy E for the M-atom 3*d* bands in M_2X compounds, showing the d_σ and d_m components and crystal-field splitting Δ.

for a Δ comparable to the width of the density of states for these bonding orbitals, a minimum in the effective M-atom radius in any of the three common structures would appear for about six to seven $3d$ electrons per molecule. The pnictides V_2X would contain seven $3d$ electrons per molecule. On the other hand, the lower half of the d_σ orbitals would be filled, or nearly so, by eleven $3d$ electrons per molecule, so a maximum effective radius is anticipated for Mn_2X.

The appearance of a second minimum in the plot of effective M-atom radius vs atomic number at 15 electrons per molecule, corresponding to Co_2X, suggests that the top of the d_σ bands is higher than the top of the d_m bands. This relation is especially reasonable for the arsenides, where the larger M–M separation weakens the M–M bonding. The existence of this second minimum also correlates well with an anomalous M_{II}-site preference energy for Ni atoms. Roger [3] has given the variations of the lattice parameters with composition for the systems $(M_{1-x}Ni_x)_2P$, where M = Cr, Mn, Fe or Co. From his data, and more convincingly from an analysis of neutron diffraction and Mössbauer spectrometry [10], it appears that, for x close to $x = 1.0$, the M atoms occupy M_I sites—whereas in general atoms of smaller electron/atom ratio occupy M_{II} sites. For x close to $x = 0$, on the other hand, the Ni atoms occupy the M_I sites; and the range of x over which the Ni atoms appear to have a strong M_I-site preference energy increases from Co to Fe to Mn to Cr. In the intermediate ranges of x there is a change of the relative site-preference energies, and the two types of ions are disordered. The anomalous site preferences of nickel are most probably due to crystal-field effects. The strong octahedral-site preference energy for a localized d^8 configuration is well known. However, electron transfer from the M atoms to the Ni atoms, which is larger the lighter the M atom, can stabilize dilute concentrations of Ni atoms in tetrahedral sites. In the system $(Cr_{1-x}Ni_x)_2P$, the Ni atoms still have a strong enough M_I-site preference at $x = 0.5$ that CrNiP is orthorhombic. In the $(Mn_{1-x}Ni_x)_2P$ system, the M_I-site preference is sufficiently weakened that the edge of the orthorhombic-phase field is at MnNiP, and in $(Fe_{1-x}Ni_x)_2P$ it is too weak for $x > 0.3$ to stabilize the orthorhombic phase for any value of x. Similarly introduction of Ni into $(Co_{1-x}Ni_x)_2P$ quenches the orthorhombic phase of Co_2P for $x > 0.1$. Conversely, the range of x over which the M atoms have a strong M_I-site preference energy decreases from Co to Fe to Mn, the all M_I-site occupancies apparently occurring in the respective ranges $0.75 \lesssim x \leqslant 1, 0.85 \lesssim x \leqslant 1$, $0.9 \lesssim x \leqslant 1$. Similarly, the crystal-field stabilizations responsible for stabilization of the orthorhombic phase in Co_2P are probably also responsible for the incomplete atomic ordering found at $x = 0.5$ in $(Fe_{1-x}Co_x)_2P$.

III. Magnetic Phase Diagrams

Since the pioneering series of papers by Hubbard [11], it has been generally appreciated that electron–electron correlation energies, where comparable to or greater than the one-electron bandwidth, will split the occupied states from the unoccupied states if there is an integral number of electrons per atom participating in band formation. In addition, these correlations introduce spontaneous magnetism. Where there are degenerate—or quasidegenerate—bands, two different correlation energies, U and U', must be distinguished. Whereas U and U' both represent the energy to add an electron to a partially filled $3d$ shell—and hence can be estimated in the free-atom limit from successive ionization potentials — addition of an electron to an orbital that is already occupied requires the energy U, and addition to an orbital that is empty the energy U'. The difference in their energies, U–U', is proportional to the intra-atomic exchange splitting Δ_{ex}. The magnitudes of these intra-atomic, electron–electron coulombic energies all decrease with increasing radial extension of the wave functions. The bandwidth w_b, on the other hand, increases with the overlap of the wave functions on neighboring atoms. Therefore, the ratio w_b/U increases unambiguously with an increase in w_b, whether this is caused by a decrease in interatomic separation or by an increase—through greater covalent mixing with an anion for example—in the radial extension of the wave function.

The most straightforward application of these ideas is to the case of a half-filled, degenerate band. Figure 8 illustrates the energy-density of states for highly correlated electrons in a half-filled, twofold-degenerate band of a simple-cubic array. Two features are important. First, the energy E_2 of the two-electron state is separated from that of the three-electron state E_3 by an energy U, since addition of a third electron per atom requires occupancy of an orbital that is already occupied. However, E_1 and E_2 are only

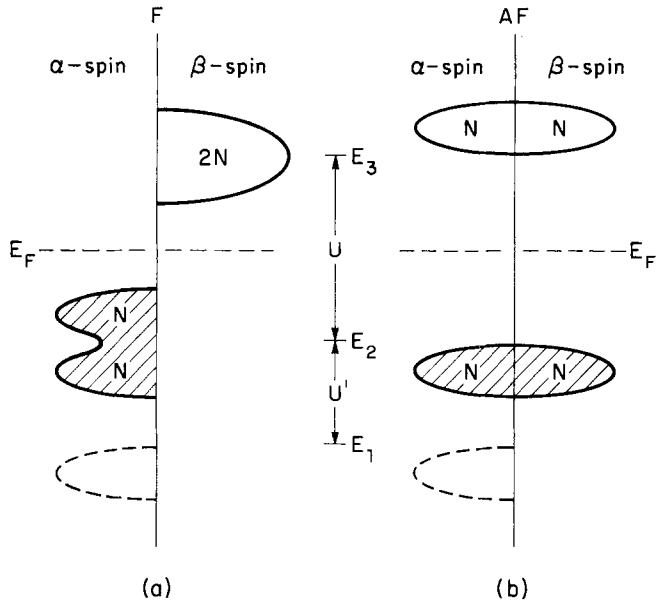

FIG. 8. Energy-density of states for half-filled, twofold-degenerate band of highly correlated electrons. (a) Ferromagnetic and (b) antiferromagnetic coupling.

separated by $U' < U$, since the addition of a second electron per atom can be accomplished by occupying empty orbitals. Second, within a band of allowed energies, the bonding orbitals lie below the reference energy E_i and the antibonding orbitals lie above it. The counterpart of an occupied bonding state of α spin is an antibonding state of β spin, of an occupied antibonding state of α spin is a bonding state of β spin, and vice versa.

Each atom carries an atomic moment as a result of the relation $U > w_b$. For $w_b/U \ll 1$, it is possible to separate the intra-atomic from the interatomic exchange interactions. The strength of the coupling between atomic moments on neighboring atoms is then given by an interatomic-exchange energy, which is the origin of the Weiss molecular-field energy kT_w. Figure 8(a) represents ferromagnetic coupling and Fig. 8(b) antiferromagnetic coupling. Ferromagnetic coupling requires that only states of one spin can be occupied. For a half-filled band, all the states of this spin are occupied, both bonding and antibonding states. Therefore, no interatomic binding energy can be achieved by ferromagnetic coupling. Antiferromagnetic coupling, on the other hand, allows states of both α and β spin to be occupied, and a half-filled band just fills all the bonding states. Therefore, binding energy can be gained by antiferromagnetic coupling, and the antiferromagnetic state is stabilized at lowest temperatures.

The origin of the antiferromagnetic coupling, like the origin of the bandwidth w_b, is the possibility of electron transfer from one atom to another. A half-filled, twofold-degenerate band has two electrons on each atom in the ground state. Electron transfer requires placing three electrons on one atom, leaving one on the near neighbor, and this costs an energy U. Therefore, electron-transfer states are excited states and mix into the ground-state wave functions via the second-order perturbation theory of superexchange. In this theory, interactions between the near-neighbor atoms of the simple-cubic array give a magnetic-ordering (Néel) temperature T_N that varies as

$$kT_N \sim zb^2/U \sim w_b^2/zU \qquad (1)$$

where z is the number of near neighbors and b is the electron-transfer energy integral. In tight-binding theory, the bandwidth is $w_b = 2zb$, and b varies as the overlap integral for orbitals on near-neighbor atoms. Antiferromagnetic coupling of all nearest neighbors is known as Type G antiferromagnetic order.

Variation of w_b and U with increasing b is shown schematically in Fig. 9. If an electron hole is introduced into the system in the range $b < b'_c$,

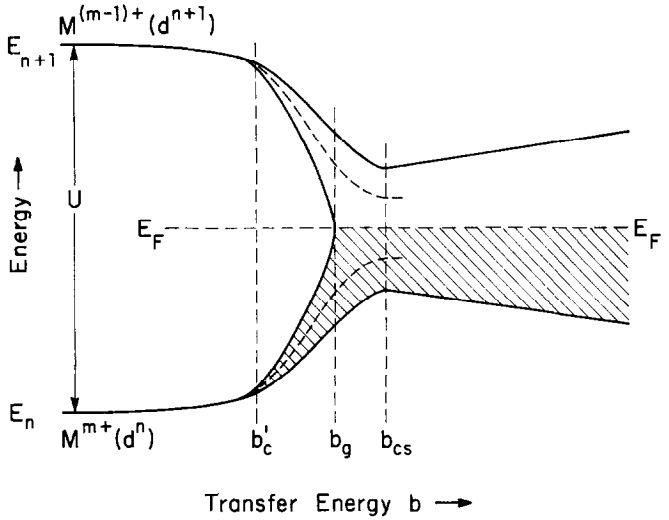

FIG. 9. Electron energies vs transfer energy b for a half-filled band.

the time for an electron to transfer from one atom to its neighbor is long compared to the period of an optical vibration, and lattice relaxations localize the hole to a single atom at any moment of time. These localized holes, called small polarons, are mobile and therefore have a finite bandwidth. However, for $b > b_c'$ screening of an electron from its nucleus by interactions with electrons on neighboring atoms increases the extension of the electron orbitals, thereby lowering U. Therefore, the ratio w_b/U should increase much more rapidly with increasing b, making the interval $b_c' < b < b_g$ relatively narrow. A semiconductor-to-metal transition occurs at b_g. For $b > b_g$, the ratio $w_b/U > 1$ increases rapidly, and conventional band theory (which assumes $U = 0$ because it is small relative to w_b) is applicable for larger b. In this domain, the half-filled band may sustain superconductivity at lowest temperatures ($T < T_{cs}$).

From these physical arguments, it is possible to construct the conceptual phase diagram shown in Fig. 10. From Eq. (1), T_N must increase monatonically with b until the perturbation expansion breaks down at a $b \approx b_c$, where $b_c' < b_c < b_m$ and b_m occurs at the critical bandwidth for spontaneous magnetism to be sustained. Within the narrow interval $b_c < b < b_m$, interatomic exchange is no longer separable, as a small perturbation, from intra-atomic exchange, and the Weiss molecular-field energy kT_w reflects both. In this domain, the Néel temperature increases with U and $dT_N/db < 0$. Where U is negligible, the Bardeen–Cooper–Schrieffer theory predicts that the superconducting transition temperature T_{cs} decreases with increasing bandwidth (decreasing density of states at the Fermi energy). As b decreases toward b_g, the energy U quenches out the superconducting state. In the magnetically ordered state ($b < b_m$), electron transfer between sublattices of opposite spin reduces the atomic moments measured by neutron diffraction. The highly correlated state ($b < b_g$) produces a larger atomic moment and hence a larger spin entropy.

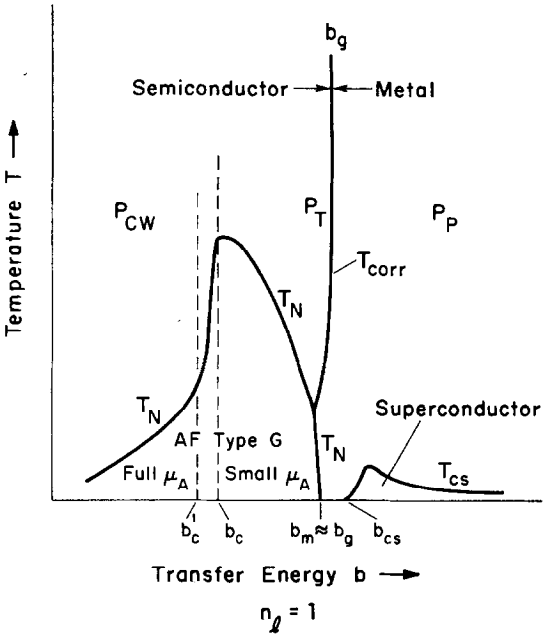

FIG. 10. Phase diagram for half-filled bands.

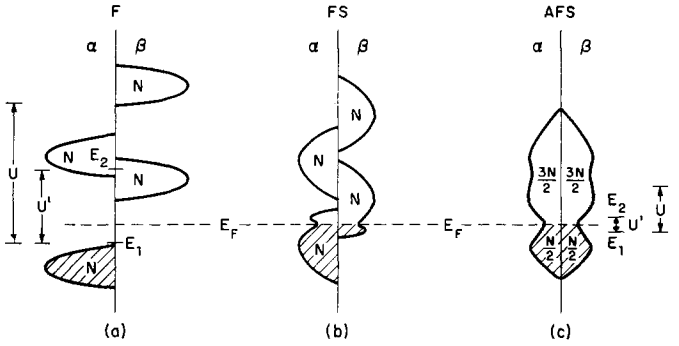

FIG. 11. Energy-density of states for quarter-filled, twofold-degenerate band of correlated electrons. (a) Strong correlations and ferromagnetic coupling. (b) Intermediate correlations and ferromagnetic spin-density wave. (c) Weak correlations and antiferromagnetic spin-density wave.

Therefore b_g increases somewhat with b at the lower temperatures, and a first-order phase change may occur at T_N in the small interval $b_g < b < b_m$ for $T < T_N$. As b increases toward b_g, thermal excitation of electrons across the energy gap makes the Weiss molecular field temperature-dependent, and the paramagnetic behavior changes from a Curie–Weiss law to temperature-independent, Pauli paramagnetism in a narrow interval of b [*12*]. More detailed discussions of the phase diagrams presented here are available elsewhere [*13*].

If the twofold-degenerate bands contain only one electron per atom, the energy-density of states is as shown in Fig. 11. It is immediately apparent that, even in the ferromagnetic state, only bonding states need be occupied. Therefore, either ferromagnetic or antiferromagnetic coupling allows binding. The binding energy associated with ferromagnetic coupling can be shown, in third-order perturbation theory, to be stronger in the limit of strong correlations, and the Curie temperature varies as

$$kT_c \sim zb^2 \Delta_{ex}/U'^2 \sim zb^2(U-U')/U'^2 \sim w_b^2(U-U')/zU'^2 \quad (2)$$

Therefore, T_c increases monotonically with b so long as the perturbation expansion is valid. However, in the simple-cubic array a Jahn–Teller distortion occurs below a $T_t > T_c$ that splits the twofold degeneracy of the localized orbitals. Degenerate orbitals of E_g symmetry would induce a distortion to tetragonal ($c/a < 1$) symmetry in which half-filled orbitals interact along the c-axis and a half-filled and an empty orbital overlap within basal planes. As a result, the magnetic ordering below T_t is antiferromagnetic Type A, which has ferromagnetic coupling in the basal planes and antiferromagnetic coupling along the c-axis. This situation is reflected in the phase diagram of Fig. 12.

Where $b > b_c' \approx b_c$, on the other hand, the coupling is ferromagnetic and there is no Jahn–Teller distortion. According to the Stoner theory of itinerant-electron ferromagnetism, the Curie temperature T_c is

$$kT_c \approx (3\sqrt{2}/\pi)\,\varepsilon_F[(kT_w/\varepsilon_F) - (2/3)]^{1/2} \quad (3)$$

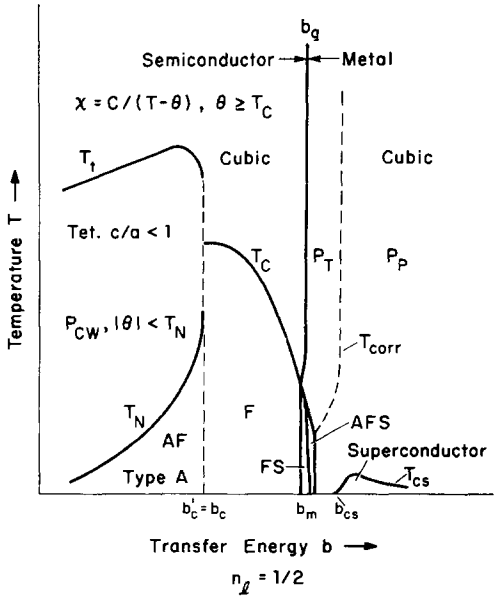

FIG. 12. Phase diagram for quarter-filled bands formed from twofold-degenerate atomic orbitals of e_g symmetry on a simple-cubic array.

where ε_F is the Fermi energy measured from the bottom (or the top for one hole per atom) of the band. It increases relatively slowly with b, whereas the Weiss molecular-field energy kT_w is an effective U that decreases more rapidly with b. Therefore T_c decreases with increasing b from a maximum near $b \approx b_c$, as indicated in Fig. 12. The Stoner theory introduces ferromagnetic intraband electron correlations that dominate where distinctions between bonding and antibonding states do not play a role.

As b increases, U' decreases and w_b increases as indicated in Fig. 11(b) and (c). The spontaneous magnetization is reduced for values of b larger than that where the up-spin and down-spin bands begin to overlap. With no overlap, spin waves are generated by the thermal excitation of down-spin states. Where down-spin electrons are present in the ground state, a standing ferromagnetic spin-density wave (FS) should be stabilized by interactions with the Fermi surface [*12*, *13*]. The net magnetization of the FS would be the simple difference between the population densities of the up-spin and down-spin bands multiplied by the Bohr magnetron μ_B.

For a large enough overlap of the up-spin and down-spin bands, an antiferromagnetic spin-density wave AFS may be stabilized relative to the FS. Metamagnetic behavior (FS to AFS transitions as a function of T and applied magnetic field H) would be observed in the transitional region. This complex transition from spontaneous ferromagnetism to Pauli paramagnetism at $b \approx b_m$ is also shown schematically in Fig. 12.

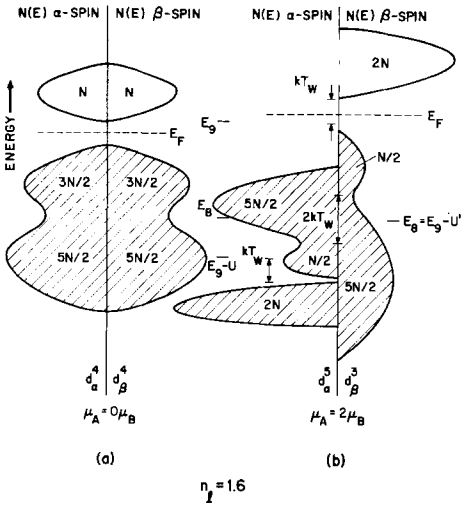

FIG. 13. Energy-density of states for fivefold-degenerate bands containing eight electrons per atom ($z_d = 8$).

Similar reasoning for fivefold-degenerate bands leads to the conceptual density-of-states N(E) vs energy curves of Figs. 13–15, which represent, respectively, the case for 8, 7.6, and 7 strongly correlated 3d electrons per atom. In each figure, a nonmagnetic state is compared with ferromagnetic states having a Weissfield stabilization kT_w. A narrowing of the bands with increased occupancy of the antibonding orbitals is also indicated. In Fig. 14, the reference energies shift

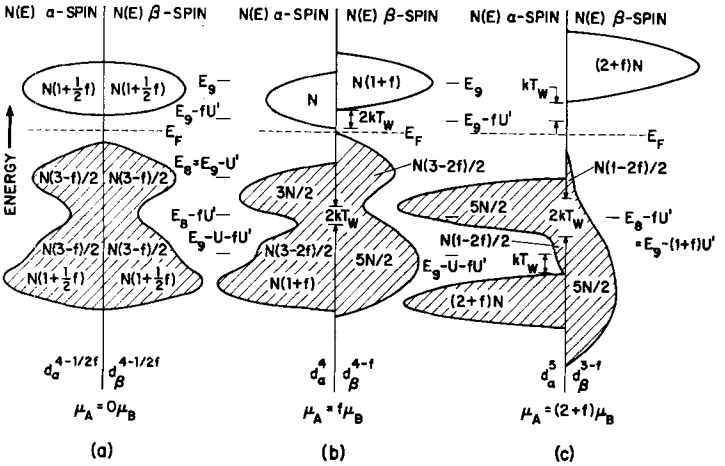

FIG. 14. Energy-density of states for fivefold-degenerate bands containing (8-f) electrons per atom. Curves drawn for $f = 0.4$, or $z_d = 7.6$.

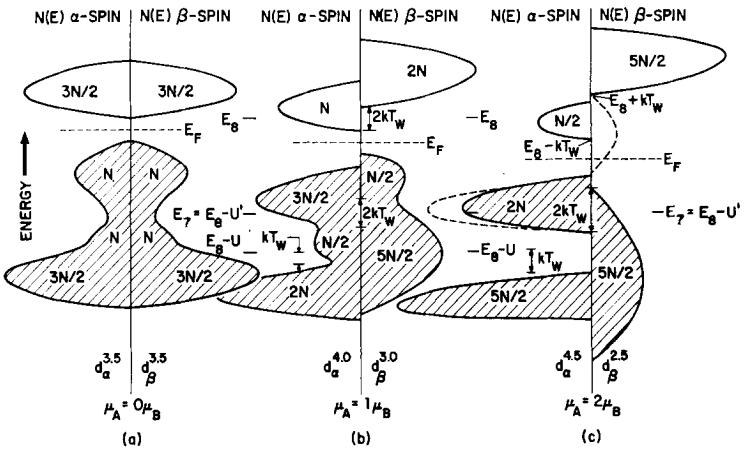

FIG. 15. Energy-density of states for fivefold-degenerate bands containing seven electrons per atom ($z_d = 7$).

with the number of holes, proceeding smoothly from E_9 to E_8. (This behavior differs from the small-polaron or localized-electron case ($b < b_c'$) shown in Fig. 16.) The antibonding hole states of one spin at reference energy E_i have their counterpart as occupied bonding states of opposite spin at a reference energy $E_i - U$. The other $3d$ electrons occupy bonding and antibonding states at a reference energy $E_i - U'$. The number of bonding states (and similarly for antibonding states) of each spin must always be $2.5N$, where N is the number of atoms. In Figs. 13(b) and 14(c), ferromagnetic coupling of all of the holes does not require placing any holes in bonding states. Therefore, ferromagnetic coupling may be stabilized, and the spontaneous magnetization at $T = 0$ K is simply the hole density multiplied by μ_B. In Fig. 15, on the other hand, ferromagnetic coupling of all of the holes would require introducing holes into bonding states—indicated by the dotted lines in Fig. 15(c). As can be seen from the figure, magnetization of the last N/2 holes would destabilize the system so long as the bandwidths are larger than $2kT_w$, which probably holds throughout the itinerant-electron domain $b > b_c$. Therefore, the spontaneous magnetization is reduced. A similar situation would occur in Fig. 14(c) for $f = n/N > 0.5$, where n is the number of holes in excess of two per atom. This finding is summarized in Fig. 17, which shows the spin-only spontaneous magnetization per atom at $T = 0$ K, μ_o, predicted for itinerant-electron ferromagnetism as a function of the number of electrons per atom z_d in the fivefold-degenerate $3d$ bands. A maximum $\mu_o = 2.5\mu_B$ occurs at 7.5 outer $3d$ electrons per atom; and $d\mu_o/dz_d$ is $+1\mu_B$ for $z_d \leqslant 7.5$, is $-1\mu_B$ for $7.5 \leqslant z_d \leqslant 1.0$. This reflects well the celebrated Slater–Pauling curve of spontaneous magnetization vs atomic number for the first-row transition metals and their alloys, provided the number of electrons per atom in overlapping s bands is assumed to be about 0.6 in the face-centered-cubic and about 1.0 in the body-centered-cubic phases. We shall use Fig. 17 to make contact with the magnetic data available for the pnictides $(M_{1-x}M_x')_2X$.

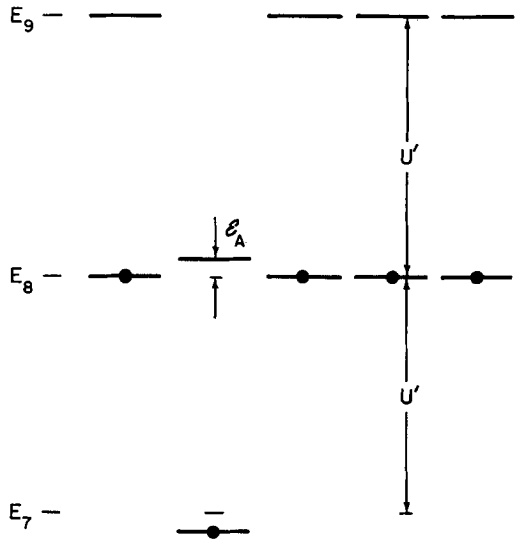

FIG. 16. Localized-electron $3d$ manifolds for $z_d = (8 - f)$.

Figures 14(b) and 15(b) illustrate states of intermediate magnetization that leave an integral

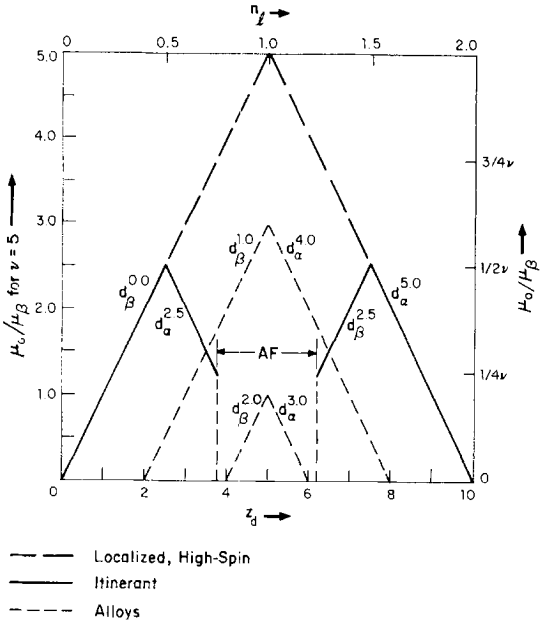

FIG. 17. Spin-only spontaneous atomic moment at $T = 0$ K, μ_0, vs $3d$-electron/atom ratio z_d for itinerant $3d$ electrons in ferromagnets. Uppermost dashed curve gives high-spin moment for localized electrons, lowest dashed curve gives weak ferromagnetic moment induced in a nonmagnetic host by magnetic impurities. Middle dashed curve gives possible ferromagnetic moment on solute atoms coupled ferromagnetically via a ferromagnetic solvent and having a d_α^n configuration matching that of solvent.

number of electrons in the α-spin band. In spontaneously magnetic compounds, such intermediate-spin states should not generally be stable relative to the saturation states of Figs. 14(c) and 15(c). Nevertheless they may be stabilized in alloys. Suppose, for example, that substitutional Co atoms containing $(8-f)$ outer $3d$ electrons were not spontaneously magnetic, but carried an atomic moment that was induced by a magnetic host. Moreover, suppose that the magnetic host was saturated with four α-spin electrons per atom, as would occur, for example, with iron atoms containing 6.5 outer $3d$ electrons $-d_\alpha^4 d_\beta^{2.5}$, similar to Fig. 14(c). Then the induced cobalt atomic moment would tend to saturate where it had a similar number of α-spin electrons, viz. at a $d_\alpha^4 d_\beta^{4-f}$ configuration. This situation seems to occur in the system $(Fe_{1-x}Co_x)_2P$.

Two additional features should be noted. First, the density-of-states vs energy curves shown in Figs. 13–15 are unlike the familiar one-electron density-of-states curves. In particular, the existence of an energy gap at E_F does not require that the system be a semiconductor. Consider the case of a nonintegral number of $3d$ electrons per atom. In the small-polaron limit, it is clear from Fig. 16(b) that an electron can jump from one atom to its nearest neighbor without expenditure of an energy U. It need only overcome a small activation energy ε_A due to the local lattice deformations that localize it. In this limit, the energies of the $3d$-electron manifolds remain at E_8 on the $(1-f)N$ atoms having eight outer $3d$ electrons and are shifted to E_7 at the fN–atoms having seven outer $3d$ electrons. In Fig. 14, on the other hand, the electrons are itinerant, so the energy of the $3d$-electron manifold shifts equally at all atoms, and the result is that E_F falls in an energy gap. However, electron antibonding states of the same spin may be interchanged across this gap at essentially no cost in energy, so the system is metallic. In the case of an integral number of $3d$ electrons per atom, on the other hand, conduction requires the creation of a hole-electron pair in the bonding bands of Fig. 11(a), and the system should be semiconducting as long as the α-spin and β-spin bands do not overlap. Spin waves reflect excited states that, like the ground state, contain an integral number of electrons per atom. Therefore these excited states are not conducting.

The second noteworthy feature is that the holes of reverse magnetization in Fig. 15(c) introduce an antiferromagnetic component to the interatomic coupling. Where the bandwidth of the α-spin states is large enough relative to $(U' + 2kT_w)$ for occupied α-spin energies to overlap the empty β–spin energies, there the reduced ferromagnetic moment F_R is not only further reduced, but also becomes a sensitive function of the bandwidth. This state I shall refer to as the FS state, by analogy with the situation in Fig. 11(b), since the densities of both α-spin and β-spin states are finite at E_F. The F_R state differs from a FS state not only because it is stable over a range of bandwidths in the interval $b_c < b < b_m$, but also because a standing spin-density wave is not stabilized by electron interaction with a Fermi surface. As the number of outer $3d$ electrons per atom is reduced from 7 to 5, the system becomes antiferromagnetic in accordance with Figs. 8–10, which illustrate the situation for half-filled bands. The domain of stability of the AFS state, through which a system would pass with increasing b on going from the FS to the paramagnetic state (see Fig. 12), increases and that of the F_R state decreases with decreasing $3d$ electron concentra-

tion. The F_R state should become unstable relative to an AFS state for all values of b where the ferromagnetic and antiferromagnetic components of the interatomic exchange are comparable, or about midway between the purely antiferromagnetic coupling (half-filled bands) and the maximum ferromagnetic coupling (three-fourths-filled bands). This occurs at a $3d$-electron/atom ratio $z_d \approx 6.25$. This transition is also marked in Fig. 17.

Finally, Fig. 17 may be generalized to any v-fold-degenerate band. Let n_l be the band-occupancy number, defined as the number of electrons per atomic orbital participating in the degenerate bands. Because of spin degeneracy, it covers the interval $0 < n_l < 2$. Thus the half-filled bands of Figs. 8–10 have $n_l = 1.0$, the quarter-filled bands of Figs. 11 and 12 have $n_l = 0.5$, and the fivefold-degenerate bands of Figs. 13–15 contain $n_l = 1.6$, 1.52 and 1.4, respectively. A maximum ferromagnetic moment $\mu_o = (v/2)\mu_B$ occurs at $n_l = 0.5$ and 1.5, antiferromagnetic order occurs at $n_l = 1.0$, and the AFS state should dominate the F_R state over the interval $0.75 \lesssim n_l \lesssim 1.25$. Over the entire ferromagnetic range, the magnetization varies with electron/atom ratio as $d\mu_o/dn_l = \pm v\mu_B$. For the fivefold-degenerate bands considered in Figs. 13–15, where $v = 5$ and $n_l = 0.2z_d$, the magnetization μ_o has the $\mu_0(\text{max}) = 2.5\mu_B$ and the $d\mu_o/dz_d = \pm 1\mu_B$ shown in Fig. 17.

IV. Interpretation of Magnetic Properties

A. The System $Fe_2P_{1-x}As_x$

Given the condition indicated in Fig. 1, the system $Fe_2P_{1-x}As_x$ contains 6.5 outer $3d$ electrons per iron atom. From Fig. 17, any spontaneous ferromagnetism of quasidegenerate $3d$ bands has a maximum spin-only saturation moment of $3.0\mu_B$ per formula unit.

In the case of Fe_2P, early measurements of the spontaneous moment μ_{mo} per formula unit at $T = 0$K have given values over the range $2.14 < \mu_{mo} < 2.76\mu_B$, depending upon the chemical impurities [*3*, *14*, *15*]. This large variability of μ_{mo} with small impurity concentrations or small deviations from stoichiometry already suggests that the moment is reduced from the predicted $3.0\mu_B$ because U is not quite large enough to saturate the α-spin bands, see Fig. 11(b). $Fe_2P_{1-x}As_x$ is the best system for testing this hypothesis, since the iron subarray remains unperturbed in first-order theory except for an increase with x in the Fe–Fe separations. The widths of the $3d$ bands should decrease sensitively with increasing Fe–Fe separation (as well as with perturbation of the cation potential), so the parameter U should increase with x. Therefore, the models of Figs. 11, 12 and 17 for Fe_2P require that in $Fe_2P_{1-x}As_x$ the moment μ_{mo} increase with x to $3.0\mu_B$ and then saturate. Roger [*3*] and Catalano, Arnott and Wold [*16*] have performed this critical experiment. They report a $d\mu_{mo}/dx > 0$ that increases with x until μ_{mo} saturates abruptly for all $x > 0.33$ at the predicted $\mu_{mo} = 3.0\mu_B$. (Roger reports a $\mu_{mo} \approx 3.25\mu_B$, but Catalano *et al.* a $\mu_{mo} \approx 3.0\mu_B$.) Furthermore, the Curie temperature T_c increases with x, or with decreasing b, as predicted qualitatively in Fig. 12. It rises from 221 K at $x = 0$ to 470 K above $x = 0.4$.

Similarly, Roger [*3*] has reported that the system $Fe_2P_{1-x}B_x$ reaches a $\mu_{mo} = 3.02\mu_B$ at $x = 0.15$, the Curie temperature increasing to $T_c = 456$ K. On the other hand, small substitutions of Mn or Cr into Fe_2P induce metamagnetic behavior. $(Fe_{1-x}Mn_x)_2P$ containing $x = 0.03$, for example, is antiferromagnetic in applied magnetic fields as high as 26 kOe [*3*]. In view of these striking changes with small substitutions of Mn and Cr, the Curie temperature and spontaneous magnetization of Fe_2P have also been studied as a function of hydrostatic pressure [*17*]. In this experiment, the bandwidth—and hence b—is expected to increase with pressure, thereby decreasing T_c until a metamagnetic state is induced; as suggested by the phase diagrams of Fig. 12 for $b \approx b_m$. The change in Curie temperature ΔT_c [°C] was found to vary with pressure P [kbar] as

$$P = -0.252(\Delta T_c) - 0.0012(\Delta T_c)^2 \qquad (4)$$

over the range $0 < P \leqslant 11$ kbar, from which a critical pressure $P_c \approx 13$ kbar may be inferred for the ferromagnetic to metamagnetic transition. Surprisingly, there was no significant change with pressure in the magnetization per molecule, μ, at 58 K. Examination of μ vs the applied field H at $T = 58$ K showed no appreciable change on passing from 1 atm to 10 kbar pressure. However, measurement of μ vs T/T_c for Fe_2P gave strikingly different results for 1 atm and 10 kbar. At $H = 10$ kOe, the inflection in μ vs T occurs at $T \approx 1.07\ T_c$ at $P = 1$ atm, but at $T \approx 1.15\ T_c$ at $P = 10$ kbar. Furthermore, an extraordinarily large exchange enhancement of the susceptibility, which extends to temperatures well above T_c, is

markedly greater at 10 kbar than at 1 atm. At $P = 10$ kbar and $T = 1.02\ T_c$, a plot of μ vs H is extremely nonlinear, resembling the initial magnetization curve of a ferromagnet at $T < T_c$. These findings indicate that hydrostatic pressure suppresses T_c much more rapidly than the paramagnetic Curie temperature θ. The situation appears to be analogous to that found in metamagnetic $Zn[Cr_2]Se_4$, where relatively small antiferromagnetic interactions at long distance induce the formation of a helicoidal spin configuration even though the near-neighbor interactions are strongly ferromagnetic. In Fe_2P the antiferromagnetic interactions at long distance may manifest a crystal-field splitting that leaves the σ-bonding orbitals half-filled, thereby creating antiferromagnetic Fe–P–Fe interactions.

Such experiments deal only with the average atomic moment per iron atom. In Fe_2P, the shorter Fe_I–Fe_I and Fe_I–P bonds (see Table I) suggest that the reduction in μ_{mo} may occur primarily at the Fe_I atoms. On the other hand, the shorter Fe_I–P bonds imply that the ratio of broad-band to 3d-core electrons is higher at Fe_I than at Fe_{II} atoms, so that the number of $3d$ electrons per Fe_I and Fe_{II} atom are, respectively, $n_I = 6.5 - \delta$ and n_{II} $6.5 + \delta$. If this is so, then from Fig. 17 it follows that in the system $Fe_2P_{1-x}As_x$ the spin density at the Fe_I sites may be smaller than that at the Fe_{II} sites over the compositional range $x > 0.33$ where $\mu_{mo} \approx 3.0\mu_B$. The atomic moments would be

$$\mu_I^{Fe} = (1.5 - \delta)\mu_B \text{ and } \mu_{II}^{Fe} = (1.5 + \delta)\mu_B \quad (5)$$

It would be interesting to investigate these predictions with neutron diffraction.

Mossbauer data of Sénateur [3] for an Fe_2P sample having $\mu_{mo} = 2.67\mu_B$ indicate a ratio $\mu_{II}^{Fe}/\mu_I^{Fe} \approx 3/2$ for the magnitudes of the atomic moments of Fe_{II} and Fe_I atoms, and hence atomic moments

$$\mu_{II}^{Fe} \approx 1.6\mu_B \text{ and } \mu_I^{Fe} \approx 1.07\mu_B \quad (5')$$

in this Fe_2P. Reduction of μ_{mo} from its theoretical value of $3.0\mu_B$ is $\Delta\mu = -0.17\mu_B$/Fe atom. Since this reduction is more likely to be sustained by the Fe_I–atom array, it follows that

$$0.1 < \delta < 0.27 \quad (6)$$

Comparison of the hyperfine fields of the Fe_{II} atoms in hexagonal Fe_2P and in orthorhombic $(Fe_{1-x}Co_x)_2P$ having $x > 0.5$, where the hyperfine fields reach a saturation value (see below), suggests that

$$\mu_{II}^{Fe}(\text{saturation}) \approx 1.67\mu_B \text{ and } \delta \approx 0.17 \quad (7)$$

B. The System $(Fe_{1-x}Co_x)_2P$

According to Fruchart *et al.* [3], the system $(Fe_{1-x}Co_x)_2P$ exhibits an hexagonal-to-orthorhombic phase change at $x = 0.16$. Within the hexagonal phase, T_c increases with x from 221 to 441 K and the magnetization μ_{mo} passes through a maximum $\mu_{mo} \approx 2.8\mu_B$ at $x \approx 0.08$. The magnetization of their Fe_2P was $\mu_{mo} = 2.67\mu_B$, and the initial slope of the magnetization vs composition curve was close to the $d\mu_{mo}/dx = 2\mu_B$ predicted from Fig. 17 for cobalt substitutions, given no change in the average iron atomic moment. However, the variation of μ_{mo} with x indicates that, as the cobalt concentration x increases, either the average cobalt moment or the average iron moment—or both—decrease. At $x = 0.16$, the magnetization has decreased to $\mu_{mo} = 2.75\mu_B$. Since the hyperfine fields obtained by Mossbauer experiments remain constant in the hexagonal phase (Sénateur, given in Roger [3]), it follows that Co–Co inter-actions suppress spontaneous magnetization of the Co atoms.

Across the hexagonal-to-orthorhombic phase change at $x \approx 0.16$, the magnetization μ_{mo} changes from 2.75 to $1.83\mu_B$ ($\Delta\mu_{mo} = -0.92\mu_B$) whereas the Curie temperature drops only 34 K, from 441 to 407 K [3]. From Mossbauer data, the drop in μ_{mo} is associated with a drop in both the Fe_{II} and the Fe_I moments. Since the molecular volume is smaller in the orthorhombic phase, the $3d$ bandwidths are larger and a drop in μ_{mo} is a necessary consequence of the model. However, the small drop in T_c is surprising, especially in view of the high-pressure results found for Fe_2P. It would appear that the suppression of T_c relative to θ in Fe_2P requires an antiferromagnetic component that tends to be reduced by the addition of β-spin electrons, which is in accord with half-filled σ–bonding orbitals in Fe_2P.

It is also reported [3] that, within the orthorhombic phase, μ_{mo} increases linearly with x in the range $0.16 < x \leqslant 0.4$, from $1.83\mu_B$ at $x = 0.20$ to a maximum of $2.02\mu_B$ at $x = 0.40$. In the range $0.4 < x \leqslant 0.8$, it decreases linearly with increasing x to $1.46\mu_B$ at $x = 0.80$. Moreover, the Mossbauer data indicate that the hyperfine field, and hence the moment, at the Fe_{II} atoms increases linearly with x in the interval $0.16 < x \leqslant 0.40$ and saturates for $x > 0.40$. The hyperfine field at the Fe_I atoms increases more slowly with x without saturating.

Interpretation of μ_{mo} for the orthorhombic phase requires an assumption about the metal-

atom ordering. From the lattice-parameter data [3], it appears that, although the initial Co atoms occupy M_I sites, the crystal-field effects enhance the relative site-preference energy of the M_{II} sites as x increases, some Co atoms occupying M_{II} sites for $x > 0.3$. Moreover, the Mossbauer data of Sénateur [3] showed that at $x = 0.5$ the M_{II} sites are 15 percent occupied by Co atoms, whereas at $x = 0.3$ there are no Co atoms on M_{II} sites. The simplest assumption for the atomic order is

$$(Fe_{1-2x}Co_{2x})_I\,Fe_{II}P \text{ for } 0.16 < x < 0.4$$

$$(Fe_{0.3-0.3x}\,Co_{0.7+0.3x})_I\,(Co_{1.7x-0.7}Fe_{1.7-1.7x})_{II}P \text{ for } 0.4 < x < 1.0.$$

For the interval $0.16 < x < 0.4$, this distribution gives

$$\mu_{mo} = \mu_{II}^{Fe} + (1-2x)\,\mu_I^{Fe} + 2x\mu_I^{Co} \quad (8)$$

and, for the interval $0.4 \leqslant x \leqslant 0.8$,

$$\mu_{mo} = (1.7\mu_{II}^{Fe} + 0.3\mu_I^{Fe})(1-x) + (0.7+0.3x)\,\mu_I^{Co} + (1.7x-0.7)\,\mu_{II}^{Co} \quad (9)$$

From Fig. 17, a spontaneous atomic moment per cobalt atom ($z_d \approx 7.5$) would have a $\mu_{Co} \approx 2.5\mu_B$ whereas an induced atomic moment would tend to saturate at $\mu_{Co} \approx 0.5\mu_B$ in order to retain the configuration $d_\alpha^{4.0}$ equal to that at the Fe atoms. Since the Co–Co interactions appear to quench any spontaneous cobalt moment in the interval $0 < x < 0.16$, only an induced atomic moment is anticipated for the cobalt atoms in the orthorhombic phase. Therefore, we assume

$$\mu_I^{Co} = (0.5-\delta')\,\mu_B \text{ and } \mu_{II}^{Co} = (0.5+\delta')\,\mu_B \quad (10)$$

Comparison of the magnitudes of the Fe_{II}–atom hyperfine fields in the hexagonal phase and in the orthorhombic phase for $x \geqslant 0.40$, where the fields are saturated, leads to the saturation Fe_{II}–atom moment of eq. (7). The Mossbauer data also indicate a ratio $\mu_{II}^{Fe}/\mu_I^{Fe} \approx 2.1$ at $x = 0.4$. It then follows from this ratio, from Eqs. (7), (8), (10), and from $\mu_{mo} = 2.02\mu_B$ that at $x = 0.4$

$$\mu_I^{Fe} \approx 0.795\mu_B,\ \mu_{II}^{Fe} \approx 1.67\mu_B,\ \mu_I^{Co} \approx 0.23\mu_B,\ \delta' \approx 0.27 \quad (11)$$

At $x = 0.2$, the ratio $\mu_{II}^{Fe}/\mu_I^{Fe} \approx 2.0$ and a $\mu_{mo} \approx 1.83\mu_B$ give, from eqs. (7), (8), (10) and $\delta' = 0.27$,

$$\mu_I^{Fe} \approx 0.66\mu_B,\ \mu_{II}^{Fe} \approx 1.32\mu_B,\ \mu_I^{Co} \approx 0.23\mu_B \quad (12)$$

The magnitude of μ_{II}^{Fe} increases linearly with x in the interval $0.16 < x \leqslant 0.40$, but saturates at $1.67\mu_B$ for $x > 0.40$. The magnitude of μ_I^{Fe} increases linearly with x without saturating, presumably following, for all $x > 0.16$, the relation—derived from Eqs. (11) and (12)—

$$\mu_I^{Fe} = 0.525 + 0.675x \quad (13)$$

If $\mu_{II}^{Fe} = 1.67\mu_B$ for $0.40 \leqslant x \leqslant 0.80$, it follows from Eqs. (9), (10) and (13) that in this interval

$$\mu_{mo} = [(3.0 - 14\delta') - (1.80 - 1.4\delta')\,x - 0.2x^2]\,\mu_B \quad (14)$$

The experimental curve for this interval appears to be described by

$$\mu_{mo}(\text{expt}) \approx [2.02 - 1.4(x-0.4)]\,\mu_B = (2.58 - 1.4x)\,\mu_B \quad (15)$$

and eq. (14) reduces, for $\delta' = 0.285$, to

$$\mu_{mo}(\text{theory}) = (2.60 - 1.4x - 0.2x^2)\,\mu_B \quad (16)$$

Thus the model and experiments are quite self-consistent with $0.27 < \delta' < 0.285$.

C. *The System* $(Fe_{1-x}Ni_x)_2P$

This system remains hexagonal for all x. In the interval $0 < x \leqslant 0.08$, where the Ni atoms enter M_I sites, the Curie temperature increases sharply with x to a maximum of 342 K at $x = 0.08$. The magnitude of μ_{mo} varies little in the interval $0 < x \leqslant 0.1$, a $\mu_{mo} = 2.73\mu_B$ being reported for $x = 0.1$. From $\mu_I^{Fe} = (1.5+\delta)\mu_B$ and $\mu_{II}^{Fe} = (1.5-\delta)\mu_B$, a $\delta = 0.17$ gives $\mu_{II}^{Fe} = 1.67\mu_B$, $\mu_I^{Fe} = 1.33\mu_B$. Therefore, a $\mu_{mo} \approx 2.73\mu_B$ implies a $\mu_{Ni} = 0\mu_B$. Thus the principal influence of the Ni atoms in this compositional interval appears to be the addition of β-spin electrons to σ-bond orbitals, and hence the elimination of the antiferromagnetic component responsible for suppressing T_c in pure Fe_2P. At larger x, on the other hand, the magnetization μ_{mo} decreases linearly from $2.73\mu_B$ at $x = 0.1$ to $0.98\mu_B$ at $x = 0.5$. This decrease is decisively more rapid than that predicted for a system containing saturated iron moments: Mossbauer data [3] give a 3 to 1 preference for iron atoms at the M_{II} sites in FeNiP, corresponding to a $\mu_{mo}(\text{saturation}) \approx 1.6\mu_B$ at $x = 0.5$. Since it is difficult to understand why the average iron atomic moment should again decrease from saturation for $x > 0.1$, it seems reasonable to suspect that the average saturation moment at the iron atoms is decreased by a transfer from the Fe-atom array of about 0.6 $3d$ electrons to each nonmagnetic Ni atom. Such a transfer is reasonable in view of the greater stability of the $3d$ bands at the heavier Ni atoms.

D. The System $CoMnP_{1-x}As_x$

Fruchart *et al.* [3] have established that the orthorhombic compound CoMnP is ordered, the Mn atoms occupying the M_{II} sites, and has a $\mu_{mo} = 3.03\mu_B$ with a $T_c = 583$ K. Nylund *et al.* [4] report that the entire system $CoMnP_{1-x}As_x$ is orthorhombic, exhibits a continuous increase with x in lattice parameters (indicating ordering of Co and Mn for all x), and is ferromagnetic with a $\mu_{mo} = 3.16\mu_B$ and a $T_c = 350$ K at $x = 1.0$.

Since the total number of $3d$ electrons per molecule is 13, the average number of $3d$ electrons per atom is 6.5, and a spin-only $\mu_{mo} = 3.0\mu_B$ follows from Fig. 17 for a ferromagnetic phase However, because Co and Mn differ by two atomic numbers, the $3d$-electron distribution is $d_\alpha^{4.0} d_\beta^{3.5+\delta'}$ and $d_\alpha^{4.0} d_\beta^{1.5-\delta^*}$ at Co and Mn, respectively. (In ordered $CoMnP_{1-x}As_x$, the relation $\delta' = \delta^*$ holds, and the average number of β-spin electrons per atom conforms to the 2.5 predicted from Fig. 17.) We anticipate a fraction δ' of a $3d$ electron is transferred to each Co atom from the Mn atoms because of the relative stability of the $3d$ bands of cobalt. The situation is analogous to that inferred for the system $(Fe_{1-x}Ni_x)_2P$. Matching of the occupancy of the α-spin bands for the two alloy components forces the presence of bonding-state holes on the Mn-atom array, and for $\delta' \leqslant 0.5$

$$\mu_I^{Co} = (0.5 - \delta')\,\mu_B,\ \mu_{II}^{Mn} = (2.5 + \delta^*)\mu_B \quad (17)$$

For $\delta' \geqslant 0.5$, $\mu_I^{Co} = 0\mu_B$.

Of particular interest in this system is the decrease with x in the Curie temperature T_c. Since the widths of the M–M $3d$ bands must decrease with increasing lattice parameter—and hence with increasing x—, this observation is superficially opposite to any prediction based on Fig. 12. However, each Mn atom carries only $(5.5 - \delta^*)$ $3d$ electrons, and holes have been forced into their bonding d_β states. Therefore, antiferromagnetic Mn–X–Mn interactions must be anticipated. The system is ferromagnetic only because the ferromagnetic Mn–Co–Mn interactions dominate the interatomic exchange. Therefore, the reduction in T_c may reflect an increase in the Mn–X–Mn coupling relative to the Mn–Co–Mn coupling. This inference can be rationalized by noting that increased M–X covalence not only enhances the M–X–M interactions, but also permits a larger δ^* and a greater crystal-field splitting of the $3d$ bands. A greater crystal-field splitting insures the antiferromagnetic character of the Mn–X–Mn interactions. The change in μ_{mo} with x suggests that δ^* increases from $\delta^* \approx 0.53$ for $x = 0$ to $\delta^* \approx 0.66$ for $x = 1.0$.

E. The System $(Co_{1-x}Mn_x)_2P$

In the system $(Co_{1-x}Mn_x)_2P$, the orthorhombic-to-hexagonal transition occurs at $x = 0.8$. The hexagonal phase ($0.8 < x \leqslant 1.0$) exhibits no spontaneous magnetism above 77 K. The orthorhombic phase, on the other hand, is ferromagnetic over the range $0.1 \leqslant x \leqslant 0.66$, although an antiferromagnetic–ferromagnetic transition occurs at a $T_1 < T_c$ (metamagnetism) in the interval $0.56 \leqslant x \leqslant 0.66$. The system is antiferromagnetic for $0.66 < x < 0.8$. The Curie temperature T_c rises with x to a maximum of 583 K at $x = 0.5$ (CoMnP), and then decreases to about 240 K at $x = 0.66$. The transition temperature T_1 increases to $T_1 = T_c \approx 240$ K at $x = 0.66$, where the magnetic-ordering temperature changes from T_c to T_N, and the rate of decrease with x in the magnetic-ordering temperature becomes significantly less for $x \geqslant 0.7$. Besides these data, Fruchart *et al.* [3] also reported that, for $x \leqslant 0.5$, the Mn atoms all occupy M_{II} sites, establishing the chemical formulae

$$Co_I(Co_{1-2x}Mn_{2x})_{II}P \text{ for } x \leqslant 0.5$$
$$(Co_{2-2x}Mn_{2x-1})_I Mn_{II}P \text{ for } x \geqslant 0.5$$

Their magnetization data gave a μ_{mo} having a linear variation $\mu_{mo} \approx (0.52 + 5.2x)\mu_B$ for $0.2 \leqslant x < 0.5$, saturating at $\mu_{mo} \approx 3.06\mu_B$ in the ferromagnetic domain $0.5 < x \leqslant 0.56$.

From the atomic distribution for $x < 0.5$, the molecular magnetization is

$$\mu_{mo} = \mu_I^{Co} + (1 - 2x)\,\mu_{II}^{Co} + 2x\mu_{II}^{Mn} \approx (0.52 + 5.2x)\,\mu_B \quad (18)$$

If the magnitudes of the atomic moments are independent of x and if $\mu_{II}^{Mn} = 3.1\mu_B$, then $\mu_I^{Co} \approx 0\mu_B$ and $\mu_{II}^{Co} \approx 0.5\mu_B$. These numbers are compatible with an induced moment on the Co_{II} atoms, but not on the Co_I atoms. Furthermore it follows that in the range $0.5 < x \leqslant 0.56$, where μ_{mo} saturates at $3.06\mu_B$, there is no induced moment on the Mn_I atoms. Therefore, we conclude that for all x spontaneous ferromagnetism is associated with the M_{II} sites and that the ferromagnetic atomic moments are

$$\mu_{II}^{Mn} \approx 3.06\mu_B,\ \mu_{II}^{Co} \approx 0.5\mu_B,\ \mu_I^{Co} \approx \mu_I^{Mn} \approx 0\mu_B \quad (19)$$

Figure 17 cannot be used to predict antiferromagnetically coupled atomic moments.

The variation of T_c with x and the metamagnetism follow qualitatively from the model: The Mn–Co–Mn interactions are strongly ferromagnetic whereas the Mn–X–Mn interactions are antiferromagnetic.

F. The Systems $(Fe_{1-x}Mn_x)CoP$ and $(Fe_{1-x}Co_x)$-MnP

Roger [3] reports that the orthorhombic system $(Fe_{1-x}Mn_x)CoP$ is ferromagnetic for all x with a linear variation in μ_{mo} from $1.87\mu_B$ at $x=0$ to $3.03\mu_B$ at $x=1$. However, the Curie temperature T_c varies differently with x in the domains $0 \leqslant x < 0.8$ and $0.8 \leqslant x \leqslant 1.0$. This may reflect a change from partial to complete ordering of the Co atoms onto M_I sites, as suggested by Roger [3]. However, $x \approx 0.8$ may also represent the composition at which $\mu_I^{Co} \to 0\mu_B$. From eqs. (7), (10) and (19) we predict a

$$\mu_{mo} \approx (0.85 + 0.2x)\mu_I^{Co} + (0.15 - 0.2x)\mu_I^{Fe} + (0.85 - 0.8x)\mu_{II}^{Fe} + x\mu_{II}^{Mn} + (0.15 - 0.2x)\mu_{II}^{Co} \quad (20)$$

for $0 \leqslant x < 0.8$, where

$$\mu_I^{Co} \approx [0.5 - (1-x)\delta' - x\delta^*]\mu_B,\ \mu_{II}^{Co} \approx 0.78\mu_B,$$
$$\mu_I^{Fe} \approx 0.85\mu_B,\ \mu_{II}^{Fe} \approx 1.67\mu_B,\ \mu_{II}^{Mn} \approx 3.06\mu_B \quad (21)$$

For $0.8 \leqslant x \leqslant 1$, on the other hand, $\mu_I^{Co} = 0\mu_B$ and

$$\mu_{mo} \approx x\mu_{II}^{Mn} + (1-x)\mu_{II}^{Fe} \quad (22)$$

Because μ_{II}^{Co} and μ_I^{Fe} have approximately the same value, the magnitude of μ_{mo} is relatively insensitive to the degree of order of the Co atoms.

Roger [3] reports that the system $(Fe_{1-x}Co_x)$-MnP is ferromagnetic only in the domain $0.8 < x \leqslant 1.0$. In the interval $0.5 < x \leqslant 0.8$ it is metamagnetic, an antiferromagnetic configuration being stabilized below a $T_t < T_c$. In the interval $0 \leqslant x < 0.5$ the system is antiferromagnetic. The molecular magnetization μ_{mo} is relatively constant in the ferromagnetic phase, decreasing from $3.03\mu_B$ at $x=1.0$ to $3.00\mu_B$ at $x=0.9$. This finding suggests that $\mu_I^{Fe} \approx 0\mu_B$ in this system and that δ^* is reduced from 0.56 for a Mn–Co pair to about 0.23 for a Mn–Fe pair.

G. Phosphide Systems Containing Chromium

Roger [3] has also investigated the influence of Cr-atom substitutions on the magnetic properties of the phosphides. He found a narrow ferromagnetic domain in the orthorhombic phase of $(Cr_{1-x}Ni_x)_2P$. In the interval $0.48 \leqslant x \leqslant 0.55$, the molecular magnetization increases from $0.62\mu_B$ at $x=0.48$ to a maximum of $0.81\mu_B$ at $x=0.50$, decreasing to $0.50\mu_B$ at $x=0.55$. In this system the Ni atoms are non-magnetic, but Cr–Ni–Cr interactions permit the appearance of a spontaneous ferromagnetism.

In the orthorhombic system $(Cr_{1-x}Mn_x)CoP$, the magnetization drops off more rapidly than linearly with increasing Cr concentration, indicating the presence of an induced moment on the Cr atoms, the magnitude of the induced moment μ_{II}^{Cr} decreasing continuously from ca. $2\mu_B$ as the number of Mn near neighbors decreases. It seems that, in phosphides, a ferromagnetic moment may be induced on Cr_{II} atoms coupled to a Ni_I atom or coupled to a Co_I atom in the presence of Mn_{II} atoms. Although the M_I atoms are without a spontaneous moment, the Cr–M_I–Cr interactions are ferromagnetic under these conditions, as would be predicted from the mean value of n_t.

V. Conclusions

From the considerations of this paper, available experimental data on the transition-metal pnictides $(M_{1-x}M'_x)_2X_{1-y}X'_y$, where X = P or As, support the following propositions:

1. Interactions between broad-band electrons lead to the condition illustrated in Fig. 1, so that the number of $3d$ electrons per molecule is known unambiguously.
2. The change of molecular volumes with M-atom atomic number in M_2X compounds reflects crystal-field splitting. The pyramidal-site preference energy for Ni atoms in large concentration is due to crystal-field effects.
3. The three related structures are stabilized by metal–metal bonding via partially filled $3d$ shells. Where the X atom is too large for three-dimensional metal–metal bonding to compete with bonding in layers, the tetragonal phase is more stable. Where metal–metal bonding is strong and the elastic restoring forces are anisotropic, the orthorhombic structure is more stable than the hexagonal structure. Anisotropic restoring forces are present in ordered MM'X compounds. In M_2X compounds, the anisotropic elastic forces required to stabilize the orthorhombic structure can only occur for special $3d$-electron concentrations that allow the less symmetric phase to advantageously remove band degeneracies, much as Jahn–Teller distortions remove orbital degeneracies.

4. From general physical arguments, it is possible to derive a universal curve of magnetization vs 3*d*-electron/atom ratio for itinerant-electron ferromagnetism. However, the change from no spontaneous ferromagnetism to spontaneous ferromagnetism proceeds via a FS state—and may also proceed by an AFS state where $0.5 < n_i < 1.5$. The FS state occurs in ferromagnetic Fe_2P. Crystal-field effects manifest themselves in an antiferromagnetic Fe–P–Fe interaction. $Fe_2P_{0.6}As_{0.4}$ is ferromagnetic with the molecular moment predicted from the universal curve. However, the atomic moments should reflect differences in 3*d*-electron density at M_I and M_{II} sites.
5. In alloys, the atomic moments must also reflect transfer of 3*d*-electron charge density from the lighter to the heavier transition-metal atoms. In the $MnCoP_{1-x}As_x$ system, both Mn and Co atoms carry four α-spin electrons and the number of β-spin electrons per molecule is 5.0, as predicted from the universal curve. Transfer of β-spin electrons from Mn to Co atoms leaves the spontaneous atomic moment entirely on the Mn atoms. In the system $(Fe_{1-x}Co_x)_2P$, there appears to be a similar stabilization of four α-spin electrons per atom, and the molecular moment is reduced from that predicted by the universal curve. In the system $(Fe_{1-x}Ni_x)_2P$, no moment is induced at the Ni atoms and the Fe atoms transfer α-spin electrons.
6. In the $(M_{1-x}M'_x)_2X$ pnictides, the M_I–M_I interactions are stronger than the M_{II}–M_{II} interactions, and the correlation energies are greater at the M_{II} atoms. Therefore, in several phosphides spontaneous atomic moments are found at M_{II} sites whereas either no moment or a weaker, induced moment is found at similar atoms at M_I sites.
7. In M_2X compounds, the smaller M_I–X separation reflects a larger broad-band electron density and a compensating, smaller 3*d*-electron density at M_I atoms. In the case M = Fe, the magnitude of the 3*d*-electron density shifted between like atoms in phosphides is $\delta \approx 0.17$ electrons per Fe_{II}–Fe_I pair. This number should increase somewhat on going to arsenides. In alloys, 3*d* electrons tend to be transferred from the lighter to the heavier element. If the lighter M_{II} atom is a near-neighbor or a next-near neighbor in the Periodic Table to the heavier M_I atom, the numbers of electrons shifted per M_{II}–M_I pair are, respectively, $\delta' \approx 0.25 \pm 0.03$ and $\delta^* \approx 0.58 \pm 0.03$ for phosphides, but may be larger (by about 0.1) in arsenides.
8. Neutron diffraction atomic moments for comparison with those predicted in Table II would contribute to the study of itinerant-electron ferromagnetism.

Acknowledgments

Thanks are due the group at Vitry, led by R. Fruchart for stimulating discussions of the extensive experimental information they have obtained on these materials.

References

1. S. Rundqvist, *Arkiv Kemi* **20**, 67 (1962).
2. T. Lundström, *Arkiv Kemi* **31**, 227 (1969).
3. R. Fruchart, A. Roger, and J. P. Sénateur, *J. Appl. Phys.* **40**, 1250 (1969); *Ann. Chim.* **4**, 79 (1969); A. Roger, Thesis, Univ. of Paris, Orsay (1970).
4. A. Nylund, A. Roger, J. P. Sénateur, and R. Fruchart, *J. Solid State Chem.* **4**, 115 (1972); Mme. Roy-Montreuil, B. Deyris, A. Michel, A. Rouault, P. L'Hértier, A. Nylund, J. P. Sénateur and R. Fruchart, *Mater. Res. Bull.* **7**, 813 (1972).
5. H. Nowotny, *Z. Anorg. Chem.* **254**, 31 (1947); S. Rundqvist, *Acta Chem. Scand.* **14**, 1961 (1960).
6. S. Geller, *Acta Cryst.* **8**, 83 (1955).
7. S. Rundqvist and F. Jellinek, *Acta Chem. Scand.* **13**, 425 (1959).
8. M. Elander, G. Hägg, and A. Westgren, *Archiv. Kemi. Min. Geol.* **12B**, 1 (1936).
9. J. B. Goodenough, "Magnetism and the Chemical Bond," Interscience and John Wiley (1963).
10. J. P. Sénateur, P. Chéritier, A. Nylund, A. Rouault, and R. Fruchart, *Mater., Res. Bull.* (in press) (1973); Y. Maeda and Y. Takashima (private communication).
11. J. Hubbard, *Proc. Roy. Soc.* (London) **A276**, 238 (1963); **A277**, 237 (1964); **A281**, 401 (1964); **A285**, 542 (1965); **A296**, 82, 100 (1966).
12. J. B. Goodenough, *J. Solid State Chem.* **3**, 26 (1971)
13. J. B. Goodenough, "Progress in Solid State Chem.," Vol. 5, (H. Reiss, Ed.) Pergamon Press, Oxford, 1971 p. 145; "Proceedings of the Winter School in Solid State Chemistry," (C. N. R. Rao, Ed.) Plenum Press, New York in press.
14. A. J. D. Meyer and M. C. Cadeville, *J. Phys. Soc. Japan* **17**, Suppl. B-1, 223 (1962).
15. D. Bellavance, J. Mikkelsen, and A. Wold, *J. Solid State Chem.* **2**, 285 (1970).
16. A. Catalano, R. J. Arnott, and A. Wold, *J. Solid State Chem.* (companion paper).
17. J. B. Goodenough, J. A. Kafalas, K. Dwight, and N. Menyuk, AIP Conf. Proc. **10**, 1973 (in press).